ATLAS NOTE

ATLAS-CONF-2014-062

24th November 2014

Search for direct production of charginos and neutralinos decaying via the 125 GeV Higgs boson in $\sqrt{s} = 8$ TeV pp collisions with the ATLAS detector

The ATLAS Collaboration

Abstract

A search for the direct pair production of charginos and neutralinos $pp \to \tilde{\chi}_1^{\pm}\tilde{\chi}_2^0$ is presented, where the chargino decays via a W boson $\tilde{\chi}_1^{\pm} \to \tilde{\chi}_1^0(W^{\pm} \to \ell^{\pm}\nu)$, while the neutralino decays via the 125 GeV Higgs boson $\tilde{\chi}_2^0 \to \tilde{\chi}_1^0(h \to bb/\gamma\gamma/\ell^{\pm}\nu qq)$ to the lightest neutralino. The final states considered for the search have large missing transverse momentum, an isolated electron or muon, and one of the following: either two jets identified as originating from bottom quarks, or two photons, or a second electron or muon with the same electric charge. The analysis is based on 20.3 fb^{-1} of $\sqrt{s} = 8$ TeV proton–proton collision data delivered by the Large Hadron Collider and recorded with the ATLAS detector. Observations are consistent with the Standard Model expectations, and limits are set in the context of a simplified supersymmetric model within which, in the case where the $\tilde{\chi}_1^0$ is massless, the direct production of $\tilde{\chi}_1^{\pm}$ and $\tilde{\chi}_2^0$ of equal mass below 250 GeV is excluded.

ATLAS-CONF-2014-062
25 November 2014

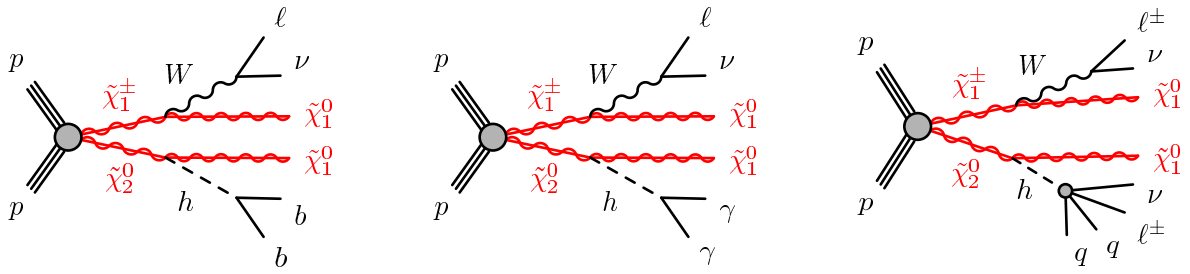

(a) One lepton and two b-quarks channel (b) One lepton and two photons channel (c) Same-sign dilepton channel

Figure 1: Diagrams for the direct production of $\tilde{\chi}_1^{\pm}\tilde{\chi}_2^0$ and the three decay modes studied in this note. For the same-sign dilepton channel (c), only the dominant decay mode is shown.

1 Introduction

Supersymmetry (SUSY) [1–9] proposes the existence of supersymmetric particles, with spin differing by one half unit with respect to that of their Standard Model (SM) partners. Charginos, $\tilde{\chi}_{1,2}^{\pm}$, and neutralinos, $\tilde{\chi}_{1,2,3,4}^0$, are the ordered mass eigenstates formed from the linear superposition of the SUSY partners of the Higgs and electroweak gauge bosons (higgsinos, winos and binos). In R-parity-conserving models [10–13], SUSY particles are pair-produced in colliders and the lightest SUSY particle (LSP) is stable. In many models it is assumed to be the $\tilde{\chi}_1^0$, which is weakly interacting. Naturalness arguments [14, 15] suggest that the lightest of the charginos and neutralinos may have masses at the electroweak scale, and the direct production of charginos and neutralinos may be accessible at the LHC.

A simplified SUSY model [16] is considered for the optimization of the search and the interpretation of results. It describes the direct production of $\tilde{\chi}_1^{\pm}$ and $\tilde{\chi}_2^0$, where the masses and the decay modes of the relevant particles ($\tilde{\chi}_1^{\pm}$, $\tilde{\chi}_1^0$, $\tilde{\chi}_2^0$) are the only free parameters. It is assumed that the $\tilde{\chi}_1^{\pm}$ and $\tilde{\chi}_2^0$ are pure wino states and degenerate in mass, while the $\tilde{\chi}_1^0$ is a pure bino state. The prompt decays $\tilde{\chi}_1^{\pm} \to W^{\pm}\tilde{\chi}_1^0$ and $\tilde{\chi}_2^0 \to h\tilde{\chi}_1^0$ are assumed to have 100% branching fractions. The Higgs boson mass is set to the measured 125 GeV and its branching ratios are assumed to be the same as in the SM. The latter assumption is motivated by those SUSY models in which the mass of the pseudo-scalar Higgs boson is much larger than the Z-boson mass.

The search presented in this note targets three Higgs boson decay modes as illustrated in Fig. 1. The Higgs boson decays either into a pair of b-quarks, or a pair of photons, or a pair of W bosons where at least one of the bosons decays leptonically. The final states therefore contain missing transverse momentum from neutrinos and neutralinos, one lepton (e or μ), and one of the following: two b-quarks (ℓbb), or two photons ($\ell\gamma\gamma$), or an additional lepton with the same electric charge ($\ell^{\pm}\ell^{\pm}$). The $h \to ZZ$ and $h \to \tau\tau$ decays also contribute to the same-sign dilepton signature.

The analysis is based on a data sample of proton–proton collisions recorded by the ATLAS detector at a centre-of-mass energy of 8 TeV. Its integrated luminosity corresponds to 20.3 fb^{-1}. Previous searches for charginos and neutralinos have been reported by ATLAS [17–19] and CMS [20, 21]. Similar searches were conducted at the Tevatron [22, 23] and LEP [24–28].

The results of this note are combined with the ATLAS search using the three-lepton and missing transverse momentum final state, performed with the same dataset [17]. The three-lepton signal regions may contain up to two hadronically decaying τ leptons providing sensitivity to the $h \to \tau\tau/WW/ZZ$ Higgs boson decay modes. The statistical combination of the results is facilitated by the fact that all

signal and control regions have been constructed not to overlap.

This note is organized in the following way: the ATLAS detector is described in Sec. 2, followed by a description of the Monte Carlo simulation in Sec. 3. In Sec. 4 the common aspects of the event reconstruction are illustrated; Sections 5, 6, and 7 describe the channel-specific features; Section 8 describes the systematic uncertainties; the results and conclusions follow in Secs. 9 and 10.

2 The ATLAS detector

ATLAS is a multipurpose particle physics experiment [29]. It consists of a detector with forward-backward symmetric cylindrical geometry.[1] The Inner Detector (ID) covers $|\eta| < 2.5$ and consists of a silicon pixel detector, a semiconductor microstrip detector, and a transition radiation tracker. The ID is surrounded by a thin superconducting solenoid providing a 2 T axial magnetic field. A high-granularity lead/liquid-argon (LAr) sampling calorimeter measures the energy and the position of electromagnetic showers within $|\eta| < 3.2$. Sampling calorimeters with LAr are also used to measure hadronic showers in the end-cap ($1.5 < |\eta| < 3.2$) and forward ($3.1 < |\eta| < 4.9$) regions, while a steel/scintillator tile calorimeter measures hadronic showers in the central region ($|\eta| < 1.7$). The muon spectrometer (MS) surrounds the calorimeters and consists of three large superconducting air-core toroid magnets, each with eight coils, a system of precision tracking chambers ($|\eta| < 2.7$), and fast trigger chambers ($|\eta| < 2.4$). A three-level trigger system selects events to be recorded for permanent storage.

3 Monte Carlo simulation

The propagation of particles through the ATLAS detector is modelled with GEANT4 [30] using the full ATLAS detector simulation [31] for all Monte Carlo (MC) simulated samples, except for the $t\bar{t}$ Powheg+Pythia and the SUSY signal samples in which the Higgs boson decays to two b-quarks, for which a fast simulation based on a parametric response of the electromagnetic and hadronic calorimeters is used [32]. The effect of multiple proton–proton collisions from the same or nearby beam bunch crossings (in-time or out-of-time pile-up) is incorporated into the simulation by overlaying additional minimum-bias events generated with Pythia8 [33] onto hard-scatter events. Simulated events are weighted to match the distribution of the average number of interactions per bunch crossing observed in data, but are otherwise reconstructed in the same manner as data.

The event generators, the accuracy of theoretical cross sections, the underlying event parameter tunes, and the parton distribution function (PDF) sets used for simulating the SM background processes are summarized in Table 1.

The SUSY signal samples are produced with Herwig++ [56] using the CTEQ6L1 PDF set. Signal cross sections are calculated at next-to-leading order (NLO) in the strong coupling constant using Prospino2 [57]. These agree with the NLO calculations matched to resummation at next-to-leading logarithmic (NLL) accuracy within ~2% [58, 59]. The nominal cross section and the uncertainty are taken respectively from the centre and the spread of the cross section predictions using different PDF sets and their associated uncertainties, as well as from variations of factorisation and renormalisation scales, as described in Ref. [60].

[1] ATLAS uses a right-handed coordinate system with its origin at the nominal interaction point (IP) in the centre of the detector and the z-axis along the beam line. The x-axis points from the IP to the centre of the LHC ring, and the y-axis points upward. Cylindrical coordinates (r, ϕ) are used in the transverse plane, ϕ being the azimuthal angle around the z-axis. The pseudorapidity is defined in terms of the polar angle θ as $\eta = -\ln\tan(\theta/2)$.

Table 1: Simulated samples used for background estimates. "Tune" refers to the choices of parameters used for the underlying event generation.

Process	Generator	Cross section	Tune	PDF set
Single top, t-channel	AcerMC [34]+Pythia [35]	NNLO+NNLL [36]	AUET2B [37]	CTEQ6L1 [38]
Single top, s-channel	Powheg [39, 40]+Pythia	NNLO+NNLL [41]	Perugia2011C [42]	CT10 [43]
tW	Powheg+Pythia	NNLO+NNLL [44]	Perugia2011C	CT10
$t\bar{t}$	Powheg+Pythia	NNLO+NNLL [45–50]	Perugia2011C	CT10
$t\bar{t}W$, $t\bar{t}Z$	MadGraph [51]+Pythia	NLO	AUET2B	CTEQ6L1
W, Z (ℓbb channel)	Sherpa [52]	NLO	–	CT10
W, Z ($\ell^{\pm}\ell^{\pm}$ channel)	Alpgen [53]+Pythia	NLO	Perugia2011C	CTEQ6L1
WW, WZ, ZZ	Sherpa	NLO	–	CT10
$W\gamma$ $W\gamma\gamma$	Alpgen+Pythia	NLO	AUET2B	CTEQ6L1
$Z\gamma$, $Z\gamma\gamma$	Sherpa	NLO	–	CT10
$W^{\pm}W^{\pm}$	Sherpa	NLO	–	CT10
Wh, Zh	Pythia8 [33]	NNLO(QCD)+NLO(EW) [54]	AU2 [55]	CTEQ6L1
$t\bar{t}h$	Pythia8	NLO(QCD) [54]	AU2	CTEQ6L1

4 Event reconstruction

The data sample considered in this analysis was collected with a combination of single-lepton, dilepton, and diphoton triggers. After applying beam, detector, and data-quality requirements, the dataset corresponds to an integrated luminosity of 20.3 fb^{-1}, with an uncertainty of 2.8%. The uncertainty is derived, following the methodology detailed in Ref. [61], from a preliminary calibration of the luminosity scale from beam-separation scans performed in November 2012.

Events are analysed if the primary vertex has five or more tracks with transverse momentum $p_{\mathrm{T}} > 400$ MeV associated with it, unless stated otherwise. For this purpose, the primary vertex of an event is identified as the vertex with the largest $\sum p_{\mathrm{T}}^2$ of associated tracks.

Electron candidates must satisfy "medium" identification criteria, following Ref. [62] (modified for 2012 data conditions), and are required to have $p_{\mathrm{T}} > 10$ GeV and $|\eta| < 2.47$. Electron p_{T} and η are determined from the calibrated clustered energy deposits in the electromagnetic calorimeter and the matched ID track, respectively.

Muon candidates are reconstructed by combining tracks in the ID and tracks or segments in the MS [63] and are required to have $p_{\mathrm{T}} > 10$ GeV and $|\eta| < 2.7$. To suppress cosmic-ray muon background, events are rejected if they contain a muon having transverse impact parameter with respect to the primary vertex $|d_0| > 0.2$ mm or longitudinal impact parameter with respect to the primary vertex $|z_0| > 1$ mm.

Photon candidates are reconstructed from clusters of energy deposits in the electromagnetic calorimeter. Clusters without matching tracks as well as those matching one or two tracks consistent with a photon conversion are considered. The shape of the cluster must match that expected for an electromagnetic shower, using criteria tuned for robustness under the pile-up conditions of 2012 [64]. The cluster energy is calibrated, separately for converted and unconverted photon candidates, using simulation. In addition, η-dependent correction factors determined from $Z \to e^+e^-$ events are applied to the cluster energy, as described in Ref. [64]. The photon candidates must have $p_{\mathrm{T}} > 20$ GeV and $|\eta| < 2.37$, excluding the gap of $1.37 < |\eta| < 1.56$ between the barrel and end-cap electromagnetic calorimeters.

Jets are reconstructed with the anti-k_t algorithm [65] with a radius parameter 0.4 using three-dimensional clusters of energy in the calorimeter [66] as input. The clusters are calibrated, weighting differently the energy deposits arising from the electromagnetic and hadronic components of the showers. The final jet energy calibration corrects the calorimeter response to the particle-level jet en-

Table 2: Summary of the overlap removal procedure. Potential ambiguities are resolved by removing nearby objects in the indicated order, from top to bottom. Different ΔR separation requirements are used in the three channels. In the same-sign channel, e^+e^- and $\mu^+\mu^-$ pairs with $m_{\ell^+\ell^-} < 12$ GeV are also removed.

Candidates	ΔR threshold			Candidate removed
	ℓbb	$\ell\gamma\gamma$	$\ell^\pm\ell^\pm$	
$e-e$	0.1	—	0.05	lowest-p_{T} e
$e-\gamma$	—	0.4	—	e
jet$-\gamma$	—	0.4	—	jet
jet$-e$	0.2	0.2	0.2	jet
$\tau-e$ or $\tau-\mu$	—	—	0.2	τ
$\mu-\gamma$	—	0.4	—	μ
e–jet or μ–jet	0.4	0.4	0.4	e or μ
$e-\mu$	0.1	—	0.1	both
$\mu-\mu$	0.05	—	0.05	both
jet$-\tau$	—	—	0.2	jet

ergy [67,68], where correction factors are obtained from simulation and then refined and validated using data. Corrections for in-time and out-of-time pile-up are also applied, as described in Ref. [69]. Events containing jets failing the quality criteria described in Ref. [67] are rejected to suppress non-collision background and events with large noise in the calorimeters.

Jets with $p_{\mathrm{T}} > 20$ GeV are considered in the central pseudorapidity ($|\eta| < 2.4$) region, and $p_{\mathrm{T}} > 30$ GeV in the forward ($2.4 < |\eta| < 4.5$) region. For central jets, information from the ID makes it possible to suppress pile-up using the "jet vertex fraction" (JVF). It is defined as the p_{T}-weighted fraction of tracks within the jet that originate from the primary vertex of the event, and it is -1 if there are no tracks within the jet. Central jets can also be tagged as originating from bottom quarks (referred to as b-jets) using the MV1 multivariate b-tagging algorithm based on quantities related to impact parameters of tracks and reconstructed secondary vertices [70]. The efficiency of the b-tagging algorithm depends on the operating point chosen for each channel, and it is reported in Secs. 5 and 7.

Hadronically decaying τ leptons are reconstructed as 1- or 3-prong hadronic jets within $|\eta| < 2.47$, and are required to have $p_{\mathrm{T}} > 20$ GeV after being calibrated to the τ energy scale [71]. Final states with hadronically decaying τ leptons are not considered here; however, they are used in the overlap removal procedure described below, as well as to make the same-sign lepton channel non-overlapping with the three-lepton search [17] that is included in the combined result.

Potential ambiguities between candidate leptons, photons and jets are resolved by removing one or both objects if they are separated by $\Delta R \equiv \sqrt{(\Delta\phi)^2 + (\Delta\eta)^2}$ below a threshold. This process eliminates duplicate objects reconstructed from a single particle, and suppresses leptons and photons contained inside hadronic jets. The thresholds and the order in which overlapping objects are removed are summarized in Table 2. The remaining leptons and photons are referred to as "preselected" objects.

Isolation criteria are applied to improve the quality of reconstructed objects. The criteria are based on the scalar sum of the transverse energies E_{T} of the calorimeter cell clusters within a radius ΔR of the object ($E_{\mathrm{T}}^{\mathrm{cone}\Delta R}$), and on the scalar sum of the p_{T} of the tracks within ΔR and associated with the primary vertex ($p_{\mathrm{T}}^{\mathrm{cone}\Delta R}$). The contribution due to the object itself is not included in either sum. The detailed values of the isolation criteria depend on the channel; they are specified in Secs. 5, 6 and 7.

The missing transverse momentum, $\vec{p}_{\mathrm{T}}^{\,\mathrm{miss}}$ (with magnitude $E_{\mathrm{T}}^{\mathrm{miss}}$), is the negative vector sum of the transverse momenta of all preselected electrons, muons, and photons as well as jets and energy of calorimeter clusters with $|\eta| < 4.9$ not associated with these objects. Clusters that are associated with electrons, photons and jets are calibrated to the scale of the corresponding objects; the ones that are not associated with any reconstructed object are calibrated at the hadronic scale [72, 73].

The efficiencies for electrons, muons, and photons to pass the reconstruction and identification criteria are measured in control samples, and corrections are applied to the simulated samples to reproduce the efficiencies in data. Similar corrections are also applied to the jet b-tagging efficiency and mis-identification probability.

5 One lepton and two b-jets channel

5.1 Event selection

The events considered in the one lepton and two b-jets channel are recorded with a combination of single-lepton triggers. The offline event selection requires exactly one signal lepton (e or μ) with $p_{\mathrm{T}} > 25$ GeV, to ensure that the event is triggered with a constant high efficiency. The signal electrons must satisfy the "tight" identification criteria of Ref. [62], $|d_0|/\sigma_{d_0} < 5$, where σ_{d_0} is the error on d_0, and $|z_0 \sin\theta| < 0.4$ mm. The signal muons must satisfy $|\eta| < 2.4$, $|d_0|/\sigma_{d_0} < 3$, and $|z_0 \sin\theta| < 0.4$ mm. The signal electrons (muons) are required to satisfy the isolation criteria $E_{\mathrm{T}}^{\mathrm{cone0.3}}/p_{\mathrm{T}} < 0.18$ (0.12) and $p_{\mathrm{T}}^{\mathrm{cone0.3}}/p_{\mathrm{T}} < 0.16$ (0.12).

Events with two or three jets are selected, where the jets can be either central ($|\eta| < 2.4$) or forward ($2.4 < |\eta| < 4.9$). Central jets have $p_{\mathrm{T}} > 25$ GeV, and forward jets have $p_{\mathrm{T}} > 30$ GeV. For central jets with $p_{\mathrm{T}} < 50$ GeV, the JVF must be > 0.5. The two highest-p_{T} central jets must be b-tagged. The chosen operating point of the b-tagging algorithm identifies b-jets in simulated $t\bar{t}$ events with an efficiency of 70%; it mis-identifies charm and light-flavour (including gluon induced) jets 20% and < 1% of the time respectively.

The dominant background contributions in the ℓbb channel are $t\bar{t}$, W + jets, and single-top Wt production. Their contributions are suppressed using the kinematic selections described below, which defines the two signal regions SRℓbb-1 and SRℓbb-2 summarized in Table 3.

The contransverse mass m_{CT} [74, 75] is defined as

$$m_{\mathrm{CT}} = \sqrt{(E_{\mathrm{T}}^{b_1} + E_{\mathrm{T}}^{b_2})^2 - |\vec{p}_{\mathrm{T}}^{\,b_1} - \vec{p}_{\mathrm{T}}^{\,b_2}|^2}, \tag{1}$$

Table 3: Selection requirements for the signal, control and validation regions of the one lepton and two b-jets channel.

	SRℓbb-1	SRℓbb-2	CRℓbb-T	CRℓbb-W	VRℓbb-1	VRℓbb-2
n_{lepton}	1	1	1	1	1	1
n_{jet}	2–3	2–3	2–3	2	2–3	2–3
$n_{b\text{-jet}}$	2	2	2	1	2	2
$E_{\mathrm{T}}^{\mathrm{miss}}$ [GeV]	> 100	> 100	> 100	> 100	> 100	> 100
m_{CT} [GeV]	> 160	> 160	100–160	> 160	100–160	> 160
m_{T}^{W} [GeV]	100–130	> 130	> 100	> 40	40–100	40–100

where $E_{\mathrm{T}}^{b_i}$ and $\vec{p}_{\mathrm{T}}^{\,b_i}$ are the transverse energy and momentum of the i-th b jet. The SM $t\bar{t}$ background has an upper endpoint at m_{CT} of approximately m_t, and is efficiently suppressed by requiring $m_{\mathrm{CT}} > 160$ GeV.

The transverse mass m_{T}^{W}, describing W candidates in background events, is defined as

$$m_{\mathrm{T}}^{W} = \sqrt{2E_{\mathrm{T}}^{\ell}E_{\mathrm{T}}^{\mathrm{miss}} - 2\vec{p}_{\mathrm{T}}^{\,\ell} \cdot \vec{p}_{\mathrm{T}}^{\,\mathrm{miss}}}, \tag{2}$$

where E_{T}^{ℓ} and $\vec{p}_{\mathrm{T}}^{\,\ell}$ are the transverse energy and momentum of the lepton. Requiring $m_{\mathrm{T}}^{W} > 100$ GeV efficiently suppresses the W + jets background. The two SRs are distinguished by $100 < m_{\mathrm{T}}^{W} < 130$ GeV for SRℓbb-1 and $m_{\mathrm{T}}^{W} > 130$ GeV for SRℓbb-2. The first signal region provides sensitivity to signal models with a mass splitting between the lightest neutralinos similar to the Higgs boson mass, while the second one targets larger mass splittings.

In each SR, events are classified into five bins of the invariant mass m_{bb} of the two b-jets as 45–75–105–135–165–195 GeV. In the SRs, about 70% of the signal events due to $h \to b\bar{b}$ populate the central bin of 105–135 GeV. The other four bins (sidebands) are used to constrain the background normalization, as described below.

5.2 Background estimation

The contributions from the $t\bar{t}$ and W + jets background sources are estimated from simulation, and normalized to data in dedicated control regions defined in the following paragraphs. The contribution from multi-jet production, where the signal lepton is a mis-identified jet or comes from a heavy-flavour hadron decay or photon conversion, is estimated using the "matrix method" described in Ref. [18], and is found to be less than 3% of the total background in all regions and is thus neglected. The remaining sources of background (single top, Z + jets, WW, WZ, ZZ, Zh and Wh production) are estimated from simulation.

Two control regions (CR), CRℓbb-T and CRℓbb-W, are designed to constrain the normalization of the $t\bar{t}$ and W + jets backgrounds respectively. The acceptance for $t\bar{t}$ events is increased in CRℓbb-T by modifying the requirement on m_{CT} to $100 < m_{\mathrm{CT}} < 160$ GeV. The acceptance of W + jets events is increased in CRℓbb-W by requiring exactly two jets, of which only one is b-tagged, and $m_{\mathrm{T}}^{W} > 40$ GeV. These two control regions are summarized in Table 3. The control regions are defined to be similar to the signal regions in order to reduce systematic uncertainties on the extrapolation to the signal regions; at the same time they are dominated by the targeted background processes and the expected signal contamination is small.

As in the signal regions, the control regions are binned in m_{bb} (m_{bj} in the case of CRℓbb-W). In the "background-only" likelihood fit, a simultaneous fit is performed to the eight m_{bb} sideband bins of the SRs and the ten m_{bb} bins of the CRs. This fit, as well as the limit setting procedure, is performed using the HistFitter package described in Ref. [76]. The two free parameters of the fit, namely the normalizations of the $t\bar{t}$ and W + jets background components, are constrained by the number of events observed in the control regions, where the number of events is described by a Poisson probability density function. The remaining nuisance parameters correspond to the systematic uncertainties described in Sec. 8. They are taken into account with their uncertainties, and adjusted to maximize the likelihood. The yields estimated with the background-only fit are reported in Table 4. While CRℓbb-T is dominated by $t\bar{t}$ events, CRℓbb-W is populated evenly by $t\bar{t}$ and W + jets events, which causes the normalisation of the $t\bar{t}$ and W + jets contributions to be negatively correlated after the fit. As a result, the uncertainties on individual background sources do not add up quadratically to the uncertainty on

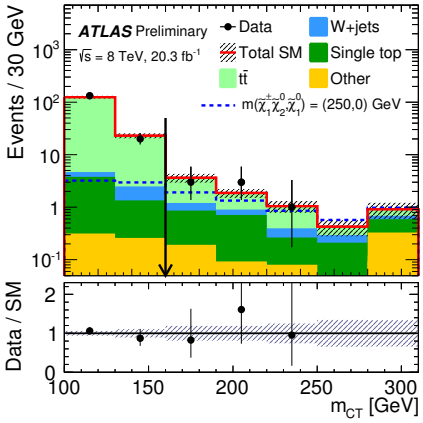

(a) m_{CT} in CRℓbb-T, SRℓbb-1 and SRℓbb-2, central m_{bb} bin

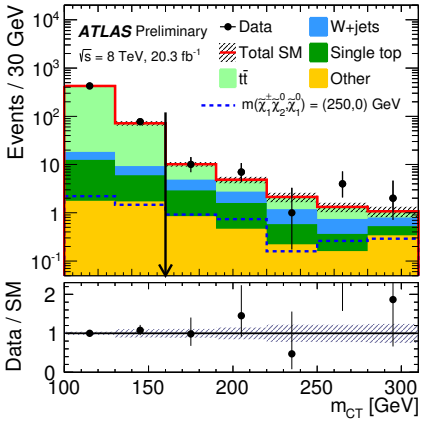

(b) m_{CT} in CRℓbb-T, SRℓbb-1 and SRℓbb-2, m_{bb} sidebands

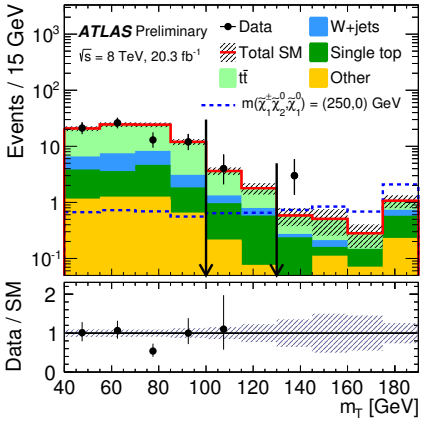

(c) m_{T}^{W} in VRℓbb-2, SRℓbb-1 and SRℓbb-2, central m_{bb} bin

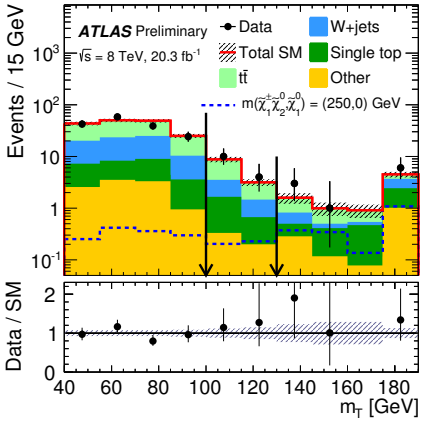

(d) m_{T}^{W} in VRℓbb-2, SRℓbb-1 and SRℓbb-2, m_{bb} sidebands

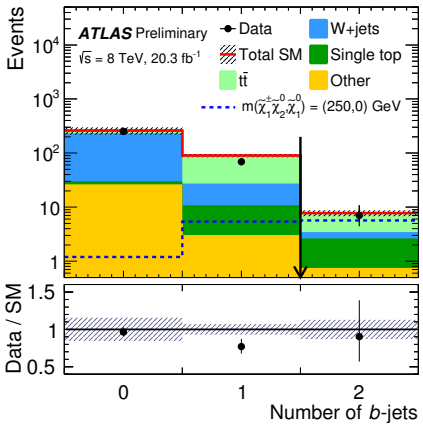

(e) $n_{b\text{-jet}}$ in SRℓbb-1 and SRℓbb-2, central m_{bb} bin

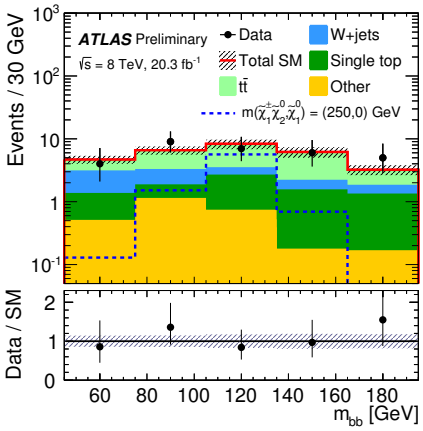

(f) m_{bb} in SRℓbb-1 and SRℓbb-2

Figure 2: Distributions of m_{CT}, m_{T}^{W}, $n_{b\text{-jet}}$ and m_{bb} for the one lepton and two b-jets channel in the indicated regions. The background histograms are obtained from the background-only fit. The hatched regions represent the total uncertainties on the background estimates. The rightmost bin in (a)–(d) includes overflow. The distributions of a signal hypothesis are also shown. The vertical arrow indicates the boundary of the signal regions. The lower panel shows the ratio between data and the SM background prediction.

Table 4: Event yields and SM expectation in the one lepton and two b-jets channel obtained with the background-only fit. "Other" includes Z + jets, WW, WZ, ZZ, Zh and Wh processes. The errors shown include statistical and systematic uncertainties.

	SRℓbb-1	SRℓbb-2	SRℓbb-1	SRℓbb-2	CRℓbb-T	CRℓbb-W	VRℓbb-1	VRℓbb-2
	$105 < m_{bb} < 135$		m_{bb} sidebands					
Observed events	4	3	14	10	651	1547	885	235
SM expectation	6.0 ± 1.3	2.8 ± 0.8	13.1 ± 2.4	8.8 ± 1.7	642 ± 25	1560 ± 40	880 ± 90	245 ± 17
$t\bar{t}$	3.8 ± 1.2	1.4 ± 0.7	8.0 ± 2.4	3.1 ± 1.4	607 ± 25	680 ± 60	680 ± 90	141 ± 18
W + jets	0.6 ± 0.3	0.2 ± 0.1	2.7 ± 0.5	1.7 ± 0.3	11 ± 2	690 ± 60	99 ± 12	62 ± 8
Single top	1.3 ± 0.4	0.7 ± 0.4	1.9 ± 0.6	2.5 ± 1.1	20 ± 4	111 ± 14	80 ± 10	27 ± 4
Other	0.3 ± 0.1	0.5 ± 0.1	0.5 ± 0.1	1.5 ± 0.2	4 ± 1	76 ± 8	16 ± 2	15 ± 1

the total SM expectation. The normalization factors are found to be 1.03 ± 0.15 for $t\bar{t}$ and 0.79 ± 0.07 for W + jets, where the errors include statistical and systematic uncertainties.

To validate the background modelling, two validation regions (VR) are defined similarly to the SRs except for requiring $40 < m_{\mathrm{T}}^{W} < 100$ GeV, and requiring $100 < m_{\mathrm{CT}} < 160$ GeV for VRℓbb-1 and $m_{\mathrm{CT}} > 160$ GeV for VRℓbb-2 as summarized in Table 3. The yields in the VRs are shown in Table 4 after the background-only fit, which does not use the data in the VRs to constrain the background. The data event yields are found to be consistent with background expectations. Figure 2 shows the distributions of m_{CT}, m_{T}^{W}, $n_{b\text{-jet}}$ and m_{bb} in various regions. The data agree well with the SM expectations in all distributions.

6 One lepton and two photons channel

6.1 Event Selection

Events recorded with diphoton triggers are used in the one lepton and two photons channel. The transverse energy thresholds at trigger level for the most energetic (leading) and second most energetic (sub-leading) photons are 35 GeV and 25 GeV, respectively. In addition, events recorded with the single-lepton triggers used for the lepton + 2 b-jet channel are included. The event selection requires exactly one signal lepton (e or μ) and exactly two signal photons, with p_{T} thresholds of 15 GeV for electrons, 10 GeV for muons, and 40 (20) GeV for leading (sub-leading) photons. The isolation criteria for both electrons and muons are $E_{\mathrm{T}}^{\mathrm{cone0.4}}/p_{\mathrm{T}} < 0.2$ and $p_{\mathrm{T}}^{\mathrm{cone0.2}}/p_{\mathrm{T}} < 0.15$. Signal photons are required to satisfy $E_{\mathrm{T}}^{\mathrm{cone0.4}} < 6$ GeV and $p_{\mathrm{T}}^{\mathrm{cone0.2}} < 2.6$ GeV.

In this channel, a neural network algorithm, based on the momenta of the tracks associated to each vertex and the direction of flight of the photons, is used to select the primary vertex, similarly to the ATLAS SM $h \to \gamma\gamma$ analysis described in Ref. [77]. Signal muons must satisfy $|d_0| < 1$ mm and $|z_0| < 10$ mm, with the impact parameters defined relative to the primary vertex.

The two largest background contributions are due to multi-jet and $Z\gamma$ production, with leptons or jets mis-reconstructed as photons. These background contributions are suppressed by requiring $E_{\mathrm{T}}^{\mathrm{miss}} > 40$ GeV.

The p_{T} of the $W \to \ell\nu$ system, reconstructed assuming background events with $p_T^{\nu} = E_{\mathrm{T}}^{\mathrm{miss}}$, is required to be back-to-back with the p_{T} of the $h \to \gamma\gamma$ candidate ($\Delta\phi(W, h) > 2.25$). Only events with a diphoton invariant mass $m_{\gamma\gamma}$ between 100 and 160 GeV are considered, and all such events are used

Table 5: Selection requirements for the signal and validation regions of the one lepton and two photons channel.

	SR$\ell\gamma\gamma$-1	SR$\ell\gamma\gamma$-2	VR$\ell\gamma\gamma$-1	VR$\ell\gamma\gamma$-2
n_{lepton}	1	1	1	1
n_γ	2	2	2	2
$E_{\text{T}}^{\text{miss}}$ [GeV]	> 40	> 40	< 40	—
$\Delta\phi(W,h)$	> 2.25	> 2.25	—	< 2.25
$m_{\text{T}}^{W\gamma_1}$ [GeV]	> 150	< 150		
	and	or	—	—
$m_{\text{T}}^{W\gamma_2}$ [GeV]	> 80	< 80		

in a signal plus background fit to the data, described in Sec. 6.2. Events in the sideband, outside the Higgs-mass window between 120 and 130 GeV, are included to constrain the non-Higgs background.

Selected events are split into two SRs with different expected signal sensitivities based on two variables $m_{\text{T}}^{W\gamma_1}$ and $m_{\text{T}}^{W\gamma_2}$, which are defined as

$$m_{\text{T}}^{W\gamma_i} = \sqrt{(m_{\text{T}}^{W})^2 + 2E_{\text{T}}^{W}E_{\text{T}}^{\gamma_i} - 2\vec{p}_{\text{T}}^{\,W}\cdot\vec{p}_{\text{T}}^{\,\gamma_i}}, \tag{3}$$

where m_{T}^{W}, E_{T}^{W} and $\vec{p}_{\text{T}}^{\,W}$ are the transverse mass, energy and momentum of the W candidate, and $E_{\text{T}}^{\gamma_i}$ and $\vec{p}_{\text{T}}^{\,\gamma_i}$ are the transverse energy and momentum of the i-th, p_T-ordered, photon. Including a photon in the transverse mass calculation provides a means to identify leptonically decaying W bosons in the presence of a final-state radiation photon. Events with $m_{\text{T}}^{W\gamma_1} > 150$ GeV and $m_{\text{T}}^{W\gamma_2} > 80$ GeV are classified into SR$\ell\gamma\gamma$-1, and those with either $m_{\text{T}}^{W\gamma_1} < 150$ GeV or $m_{\text{T}}^{W\gamma_2} < 80$ GeV into SR$\ell\gamma\gamma$-2. SR$\ell\gamma\gamma$-1 provides the most sensitivity to the signal, while SR$\ell\gamma\gamma$-2 assists in constraining systematic uncertainties.

Two overlapping validation regions are defined by inverting and relaxing the $E_{\text{T}}^{\text{miss}}$ and $\Delta\phi(W,h)$ cuts relative to those of the signal regions. The first region VR$\ell\gamma\gamma$-1 requires $E_{\text{T}}^{\text{miss}} < 40$ GeV and no cut on $\Delta\phi(W,h)$, and the second region VR$\ell\gamma\gamma$-2 requires $\Delta\phi(W,h) < 2.25$ and no cut on $E_{\text{T}}^{\text{miss}}$. The signal and validation regions are summarized in Table 5.

The distributions in the Higgs window of the four kinematic variables used to define the SRs are shown in Fig. 3. For illustration purposes, the observed yield in the sideband region is shown for each distribution, scaled into the Higgs window by the relative widths of the sideband and Higgs window, 10 GeV / 50 GeV = 0.2. Also shown, in each plot, is a simulation-based cross check of the background estimate. To reduce statistical uncertainties originating from the limited number of simulated events, the non-Higgs contributions are obtained in the Higgs sideband and scaled into the Higgs window by 0.2. The simulation-based prediction of the non-Higgs background is estimated from the W/Z(γ, $\gamma\gamma$)+jets samples, after applying a data-driven correction for the probability of electrons or jets to be reconstructed as photons. A small contribution from backgrounds with jets reconstructed as leptons is determined by using the 'fake factor' method [78]. This simulation-based background estimate is only used as a cross check of the data sideband background estimate described below. It shows consistent results with the data estimate, but it is not used for limit setting.

6.2 Background estimation

The contribution from background sources that do not contain a $h \to \gamma\gamma$ decay can be statistically separated by a template fit to the $m_{\gamma\gamma}$ distribution. A similar approach is followed as in Ref. [77]: the

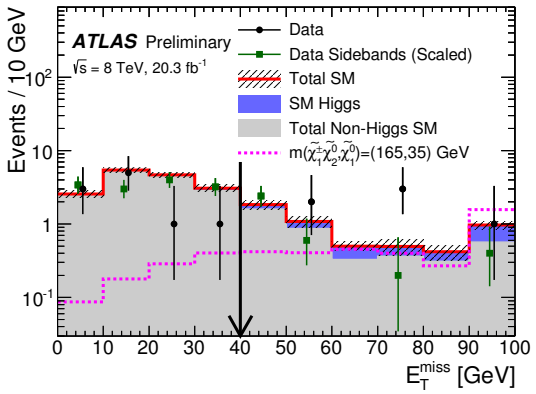

(a) $E_{\mathrm{T}}^{\mathrm{miss}}$in SR$\ell\gamma\gamma$-1 and SR$\ell\gamma\gamma$-2

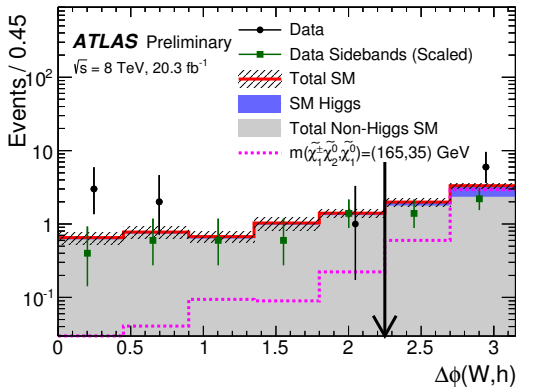

(b) $\Delta\phi(W,h)$ in SR$\ell\gamma\gamma$-1 and SR$\ell\gamma\gamma$-2

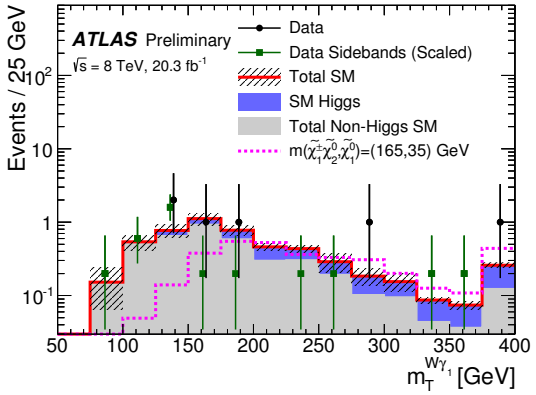

(c) $m_{\mathrm{T}}^{W\gamma_1}$ in SR$\ell\gamma\gamma$-1 and SR$\ell\gamma\gamma$-2

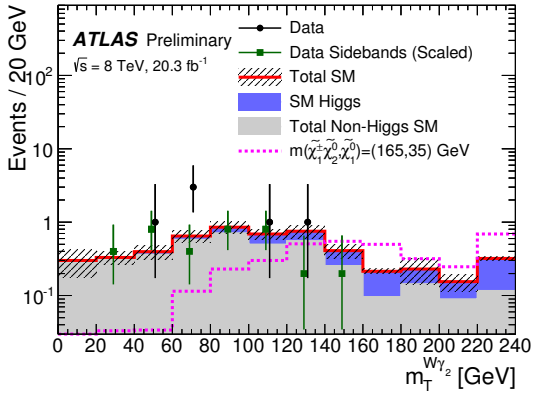

(d) $m_{\mathrm{T}}^{W\gamma_2}$ in SR$\ell\gamma\gamma$-1 and SR$\ell\gamma\gamma$-2

Figure 3: Distributions of $E_{\mathrm{T}}^{\mathrm{miss}}$, $\Delta\phi(W,h)$, $m_{\mathrm{T}}^{W\gamma_1}$ and $m_{\mathrm{T}}^{W\gamma_2}$ in the one lepton and two photons signal regions for the Higgs window ($120 < m_{\gamma\gamma} < 130$ GeV). The selections on $E_{\mathrm{T}}^{\mathrm{miss}}$ and $\Delta\phi(W,h)$ have been removed for these distributions; their positions are indicated by arrows. The filled and hashed regions represent the yield and total uncertainties on the simulation-based background cross check. The contributions from non-Higgs backgrounds are scaled by 10 GeV / 50 GeV = 0.2 from the $m_{\gamma\gamma}$ sideband ($100 < m_{\gamma\gamma} < 120$ GeV and $130 < m_{\gamma\gamma} < 160$ GeV) into the Higgs window. The rightmost bin in (a), (c), and (d) includes overflow. Scaled data in the sideband are shown as squares, while events in the Higgs window are shown as circles. The distributions of a signal hypothesis are also shown.

non-Higgs background is modeled as $\exp(-\alpha m_{\gamma\gamma})$, with the decay constant α as a free, positive parameter in the fit. Alternate functional models are used to evaluate the systematic uncertainty due to the choice of background modelling function. The $h \to \gamma\gamma$ template, used for the Higgs background and signal, is defined by the sum of a Crystal Ball function [79] for the core of the distribution and a Gaussian function for the tails. This functional form follows the one used in the SM $h \to \gamma\gamma$ analysis [77], with the nominal values and uncertainties of the fit parameters determined by fits to the simulation in SR$\ell\gamma\gamma$-1 and SR$\ell\gamma\gamma$-2. The results of the fit to the simulation are used as an external constraint on the template during the fit to data. The width of the Gaussian core of the Crystal Ball quantifies the detector resolution and is determined in simulation to be approximately 3 GeV. This is comparable to the resolution found in the SM $h \to \gamma\gamma$ analysis [77].

Table 6: Event yields and SM expectation in the Higgs window of the lepton plus two photon channel ($120 < m_{\gamma\gamma} < 130$ GeV) after the background-only fit. The Higgs window is excluded from the fit in the two signal regions. The errors shown include statistical and systematic uncertainties.

	SR$\ell\gamma\gamma$-1	SR$\ell\gamma\gamma$-2	VR$\ell\gamma\gamma$-1	VR$\ell\gamma\gamma$-2
Observed events	1	5	30	26
SM expectation	1.6 ± 0.4	3.3 ± 0.8	30.2 ± 2.3	20.4 ± 1.9
Non-Higgs	0.6 ± 0.3	3.0 ± 0.8	29.2 ± 2.3	19.8 ± 1.9
Wh	0.85 ± 0.02	0.23 ± 0.01	0.71 ± 0.02	0.29 ± 0.01
Zh	0.04 ± 0.01	0.02 ± 0.01	0.14 ± 0.02	0.05 ± 0.01
$t\bar{t}h$	0.14 ± 0.01	0.02 ± 0.01	0.11 ± 0.01	0.25 ± 0.01

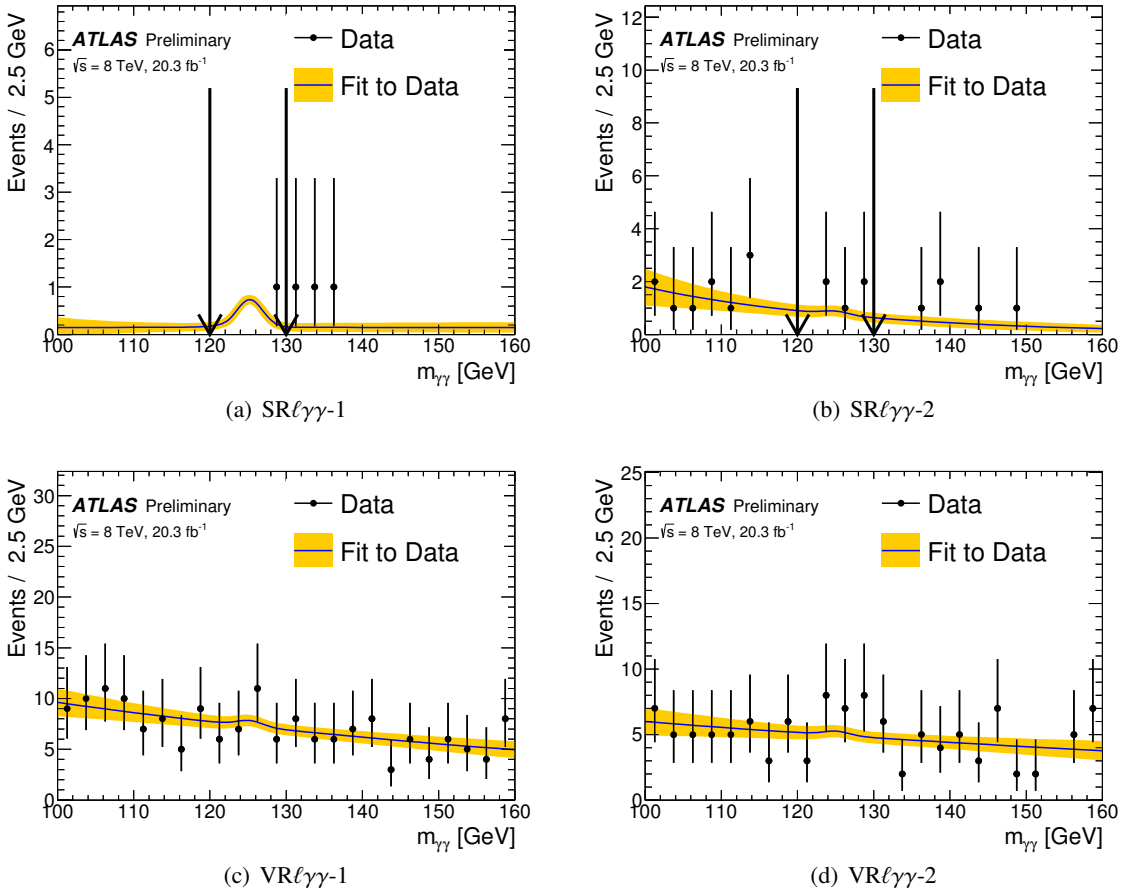

(a) SR$\ell\gamma\gamma$-1

(b) SR$\ell\gamma\gamma$-2

(c) VR$\ell\gamma\gamma$-1

(d) VR$\ell\gamma\gamma$-2

Figure 4: Results of the background-only fit to the $m_{\gamma\gamma}$ distribution in the one lepton and two photons signal and validation regions. The contributions from SM Higgs boson production are constrained to the MC prediction and associated systematic uncertainties. The band shows the systematic uncertainty in the fit. The fit is performed on events with 100 GeV $< m_{\gamma\gamma} <$ 160 GeV, with events in SR$\ell\gamma\gamma$-1 or SR$\ell\gamma\gamma$-2 in the Higgs window (120 GeV $\leq m_{\gamma\gamma} \leq$ 130 GeV), indicated by the arrows, excluded from the fit.

Contributions from SM processes with a real Higgs boson decay are estimated by simulation and come primarily from Wh associated production, followed by $t\bar{t}h$ and Zh. Systematic uncertainties on the signal yield of these SM processes are discussed in Sec. 8. Figure 4 shows the background-only fits to the observed $m_{\gamma\gamma}$ distributions in the signal and validation regions, with the signal region Higgs window ($120 < m_{\gamma\gamma} < 130$ GeV) excluded from the fit. Table 6 summarizes the observed event yields in the Higgs window and the background estimates in the signal and validation regions. The errors are dominated by the statistical uncertainty due to the number of events in the $m_{\gamma\gamma}$ sidebands.

7 Same-sign dilepton channel

7.1 Event Selection

Events recorded with a combination of dilepton triggers are used in the same-sign dilepton channel. The lowest unprescaled trigger p_{T} thresholds depend on the flavour of the leptons and are at most 25 GeV and 14 GeV for the leading and sub-leading lepton, respectively. The offline event selection requires two same-sign signal leptons (ee, $e\mu$ or $\mu\mu$) with $p_{\mathrm{T}} > 30$ GeV and 20 GeV and no additional preselected lepton. The signal electrons must satisfy the "tight" identification criteria from Ref. [62], $|d_0|/\sigma_{d_0} < 3$, and $|z_0 \sin\theta| < 0.4$ mm. The signal muons must satisfy $|\eta| < 2.4$, $|d_0|/\sigma_{d_0} < 3$, and $|z_0 \sin\theta| < 1$ mm. The isolation criteria for electrons (muons) are $E_{\mathrm{T}}^{\mathrm{cone0.3}}/\min(p_{\mathrm{T}}, 60\ \mathrm{GeV}) < 0.13$ (0.14) and $p_{\mathrm{T}}^{\mathrm{cone0.3}}/\min(p_{\mathrm{T}}, 60\ \mathrm{GeV}) < 0.07$ (0.06). Events containing a hadronically decaying preselected τ lepton are rejected in order to avoid statistical overlap with the three-lepton final states [17].

Events are required to contain between one and three central ($|\eta| < 2.4$) jets with $p_{\mathrm{T}} > 20$ GeV and $|\mathrm{JVF}| > 0$ if $p_{\mathrm{T}} < 50$ GeV. To reduce backgrounds with heavy-flavour decays, all the jets must fail the b-tagging criteria at the 80% efficiency operating point. There must be no forward ($2.4 < |\eta| < 4.9$) jet with $p_{\mathrm{T}} > 30$ GeV.

The dominant background contributions in the $\ell^{\pm}\ell^{\pm}$ channel are due to SM diboson production (WZ and ZZ) leading to two "prompt" leptons and to events with "non-prompt" leptons (heavy-flavour decays, photon conversions and mis-identified jets). These backgrounds are suppressed with the tight identification criteria described above, and with the kinematic requirements summarized in Table 7. The requirements have been optimized separately for each lepton flavour combination (ee, $\mu\mu$, and $e\mu$), and for different numbers of reconstructed jets, leading to six signal regions.

The dilepton invariant mass $m_{\ell\ell}$ is required to differ by at least 10 GeV from the Z-boson mass for the ee channel, in which contamination due to electron charge mis-identification is significant.

The visible mass of the Higgs boson candidate is defined for the 1-jet signal regions as the invariant mass ($m_{\ell j}$) of the jet and the lepton that is closest to it in terms of ΔR, and for the two-or-three-jet signal regions as the invariant mass ($m_{\ell jj}$) of the two highest-p_{T} jets and the lepton that is closest to them as a system. In the signal regions, the cut $m_{\ell j} < 90$ GeV is required for SR$\ell\ell$-1 and the cut $m_{\ell jj} < 120$ GeV for SR$\ell\ell$-2.

Depending on the final state additional kinematic variables are used to further reduce the background. Requiring the pseudorapidity difference between the two leptons $\Delta\eta_{\ell\ell} < 1.5$ decreases the WZ and ZZ background. Requirements on $E_{\mathrm{T}}^{\mathrm{miss,rel}}$, defined as

$$E_{\mathrm{T}}^{\mathrm{miss,rel}} = \begin{cases} E_{\mathrm{T}}^{\mathrm{miss}} & \text{if } \Delta\phi > \pi/2, \\ E_{\mathrm{T}}^{\mathrm{miss}} \sin(\Delta\phi) & \text{if } \Delta\phi < \pi/2, \end{cases} \tag{4}$$

where $\Delta\phi$ is the azimuthal angle difference between $\vec{p}_{\mathrm{T}}^{\,\mathrm{miss}}$ and the nearest lepton or jet, reduce the Z + jets and non-prompt lepton background in the ee channel. The $E_{\mathrm{T}}^{\mathrm{miss,rel}}$ is defined to reduce the impact

Table 7: Selection requirements for the signal regions of the same-sign dilepton channel.

	SRee-1	SRee-2	SR$\mu\mu$-1	SR$\mu\mu$-2	SR$e\mu$-1	SR$e\mu$-2
Lepton flavours	ee	ee	$\mu\mu$	$\mu\mu$	$e\mu$	$e\mu$
n_{jet}	1	2 or 3	1	2 or 3	1	2 or 3
Leading lepton p_{T} [GeV]	> 30	> 30	> 30	> 30	> 30	> 30
Subleading lepton p_{T} [GeV]	> 20	> 20	> 20	> 30	> 30	> 30
$\lvert m_{\ell\ell} - m_Z \rvert$ [GeV]	> 10	> 10	–	–	–	–
$\Delta\eta_{\ell\ell}$	–	–	< 1.5	< 1.5	< 1.5	< 1.5
$E_{\text{T}}^{\text{miss,rel}}$ [GeV]	> 55	> 30	–	–	–	–
m_{eff} [GeV]	> 200	–	> 200	> 200	> 200	> 200
$m_{\text{T}}^{\text{max}}$ [GeV]	–	> 110	> 110	–	> 110	> 110
$m_{\ell j}$ or $m_{\ell jj}$ [GeV]	< 90	< 120	< 90	< 120	< 90	< 120

on $E_{\text{T}}^{\text{miss}}$ of any potential mis-measurement, either from jets or from leptons. The scalar sum m_{eff} of the transverse energies of the leptons, jets and the missing transverse momentum is used to suppress the diboson background. Requiring $m_{\text{T}}^{\text{max}} > 110$ GeV, where $m_{\text{T}}^{\text{max}}$ is the larger of the two m_{T}^{W} values computed with one of the leptons and the missing transverse momentum, suppresses background events with one leptonically decaying W boson, whose transverse mass distribution has an end-point at m_W.

7.2 Background estimation

The irreducible background in the same-sign dilepton channel is dominated by WZ and ZZ diboson productions, in which both vector bosons decay leptonically and one or two leptons do not satisfy the selection requirements, mostly the kinematic ones. These contributions are estimated from the simulation.

Background contributions due to non-prompt leptons are estimated with the matrix method. It takes advantage of the difference between the efficiencies for prompt and non-prompt leptons, defined as the fractions of prompt and non-prompt preselected leptons, respectively, that pass the signal-lepton requirements. The number of events containing non-prompt leptons is obtained from these efficiencies and the observed number of events in each SR or VR using four categories of selection with preselected or signal leptons. The efficiencies for prompt and non-prompt leptons are derived, as a function of p_{T} and η, for each process leading to either prompt or non-prompt leptons using the truth information from simulated events. They are then corrected with simulation-to-data scale factors measured in control regions, as described in Ref. [18]. The contributions from each process leading to either prompt or non-prompt leptons are then used to compute a weighted-average efficiency, where the weight for each process is determined as its relative contribution to the number of preselected leptons in the region of interest.

Same-sign background events where the lepton charge is mis-measured are usually due to a hard bremsstrahlung photon with subsequent asymmetric pair production. The charge mis-measurement probability, which is negligible for muons, is measured in data as a function of electron p_{T} and $|\eta|$ using events from the $Z \to e^+e^-$ sample where the two electrons are reconstructed with the same sign. Such probability, which is below 1% for most of the p_{T} and η values, is then applied to the simulated opposite-sign ee and $e\mu$ pairs to estimate this background [80]. Although any process with the $e^\pm e^\mp$ or $e^\pm\mu^\mp$ final state can mimic the same-sign signature with charge mis-measurement, most of this background contribution is due to the production of Z + jets events, amounting to less than 10% of

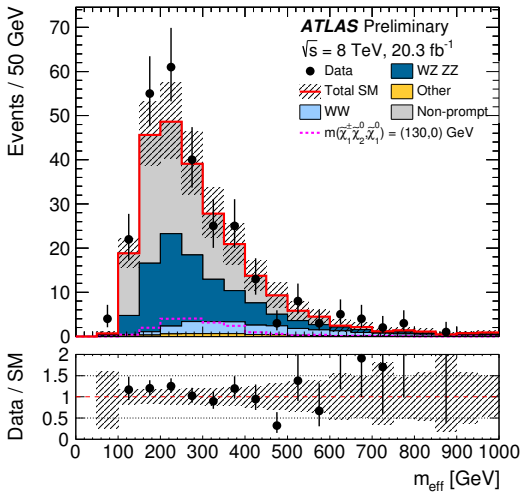

Figure 5: Distribution of m_{eff} in the validation region of the same-sign $e\mu$ channel. This validation region is defined by applying only the n_{jet} and p_{T} requirements from Table 7, and reversing the $m_{\ell j}$, $m_{\ell jj}$ criteria. The hashed regions represent the total uncertainties on the background estimates. The distribution of a signal hypothesis is also shown. The lower panel shows the ratio between data and the SM background prediction.

the background yield in any of the $\ell^{\pm}\ell^{\pm}$ signal regions.

Estimates of non-prompt lepton and charge mis-measurement background are tested in validation regions obtained by applying only the n_{jet} and p_{T} requirements from Table 7 and requiring $m_{\ell j} > 90$ GeV or $m_{\ell jj} > 120$ GeV. The number of observed events agrees with the expected background in all validation regions. Figure 5 shows the distribution of m_{eff} in the validation region of the same-sign $e\mu$ channel. The number of observed and expected events in each signal region is reported in Table 8. Figure 6 shows the m_{eff}, $m_{\text{T}}^{\text{max}}$, $m_{\ell j}$, and $m_{\ell jj}$ distributions in the same-sign dilepton signal regions. No significant excess is observed over the SM background expectations in any channel.

Table 8: Event yields and SM expectation in the same-sign dilepton channel signal regions. The WW background includes both $W^{\pm}W^{\pm}$ and $W^{\pm}W^{\mp}$ production, the latter due to electron charge mis-measurement. "Other" background includes $t\bar{t}$, single top, Z + jets, Zh and Wh production. The errors shown include statistical and systematic uncertainties.

	SRee-1	SRee-2	SR$\mu\mu$-1	SR$\mu\mu$-2	SR$e\mu$-1	SR$e\mu$-2
Observed events	2	1	6	4	8	4
SM expectation	6.0 ± 1.2	2.8 ± 0.8	3.8 ± 0.9	2.6 ± 1.1	7.0 ± 1.3	1.9 ± 0.7
Non-prompt	3.4 ± 1.0	1.6 ± 0.5	0.00 ± 0.20	0.3 ± 0.4	3.0 ± 0.9	0.48 ± 0.28
WZ, ZZ	2.2 ± 0.6	0.7 ± 0.4	3.4 ± 0.8	1.8 ± 0.9	3.3 ± 0.8	1.1 ± 0.5
WW	0.33 ± 0.31	0.22 ± 0.23	0.24 ± 0.29	0.4 ± 0.5	0.4 ± 0.4	0.23 ± 0.26
Other	0.13 ± 0.13	0.31 ± 0.31	0.14 ± 0.14	0.06 ± 0.06	0.19 ± 0.17	0.09 ± 0.08

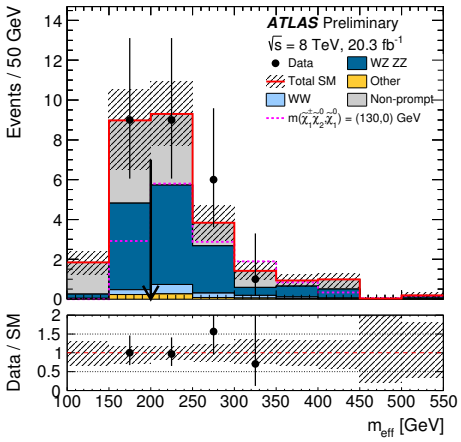

(a) m_{eff} in SR$\ell\ell$-1

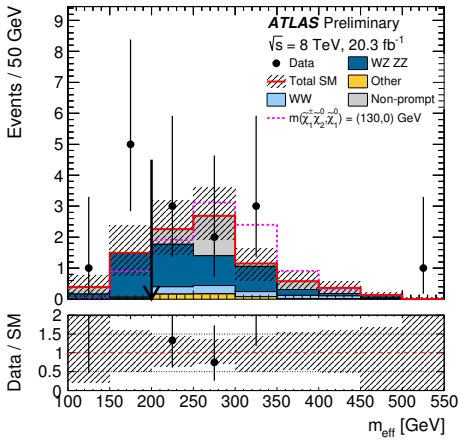

(b) m_{eff} in SR$\ell\ell$-2

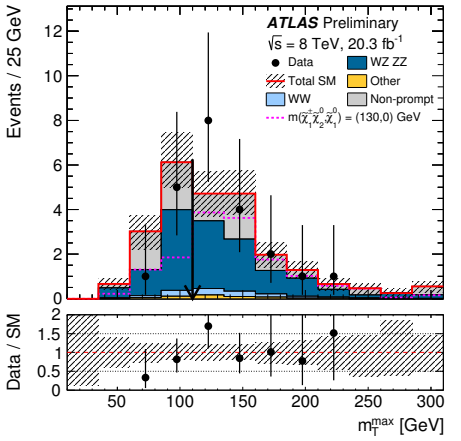

(c) $m_{\text{T}}^{\text{max}}$ in SR$\ell\ell$-1

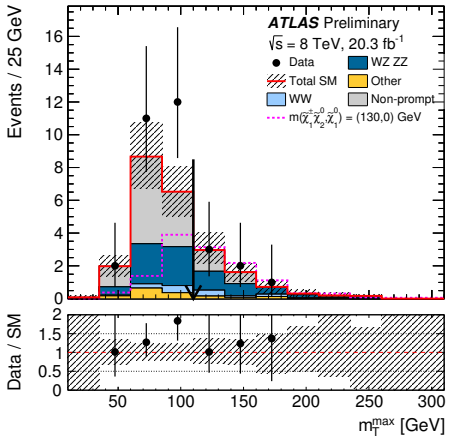

(d) $m_{\text{T}}^{\text{max}}$ in SR$\ell\ell$-2

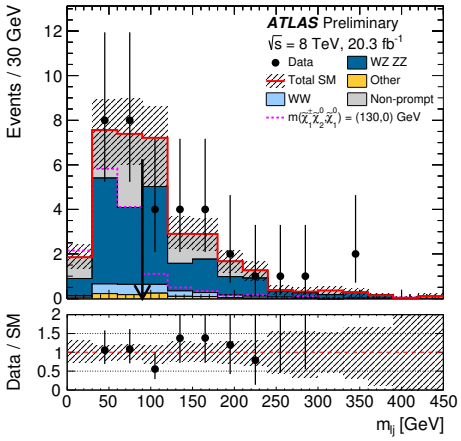

(e) $m_{\ell j}$ in SR$\ell\ell$-1

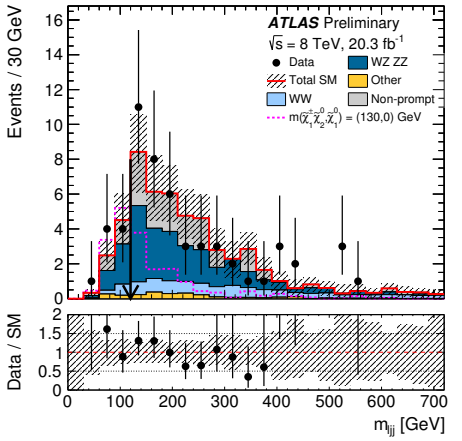

(f) $m_{\ell jj}$ in SR$\ell\ell$-2

Figure 6: Distributions of m_{eff}, $m_{\text{T}}^{\text{max}}$, $m_{\ell j}$ and $m_{\ell jj}$ for the same-sign dilepton channel in the signal regions with 1-jet (left) and 2-or-3-jet (right). SR$\ell\ell$-1 is the sum of SRee-1, SR$e\mu$-1, and SR$\mu\mu$-1; SR$\ell\ell$-2 is the sum of SRee-2, SR$e\mu$-2, and SR$\mu\mu$-2. All selection criteria are applied, except for the one on the variable being shown. The value of the cut, which may not be applied in all flavor channels, is indicated by the vertical arrow. The hashed regions represent the total uncertainties on the background estimates. The distributions of a signal hypothesis are also shown. The lower panel shows the ratio between data and the SM background prediction. The rightmost bin of each plot includes overflow.

8 Systematic uncertainties

Table 9 summarizes the contributions of the dominant sources of systematic uncertainties on the total expected background yields in the six signal regions.

For the one lepton and two b-jets channel, theoretical uncertainties of the $t\bar{t}$ and single-top background estimates are the most important. They are evaluated by comparing different generators (POWHEG, MC@NLO and ACERMC) and parton shower algorithms (PYTHIA and HERWIG), varying the QCD scales up and down by a factor of two, and taking the envelope of the background variations when using different PDF sets. Statistical uncertainties from the data in the CRs result in uncertainties on the normalization of the $t\bar{t}$ and W + jets backgrounds, while the limited number of simulated events yields uncertainty on the shape of the background m_{bb} distributions. Experimental systematic uncertainties are dominated by the uncertainties on the jet energy scale [68] and resolution [81], that are derived from a combination of test-beam data and in-situ measurements, and followed by the uncertainty on the b-jet identification [82].

For the one lepton and two photons channel, the background uncertainties are dominated by the data statistics in the $m_{\gamma\gamma}$ sidebands. The only source of systematic uncertainty on the non-Higgs background estimate is the choice of the $m_{\gamma\gamma}$ model. The systematic uncertainties on the Higgs background estimates are dominated by the theoretical uncertainties on the Wh, Zh, and $t\bar{t}h$ production cross sections and the photon reconstruction. The main theoretical uncertainties arise from QCD scale variations and from parton distribution functions [54]. Scale variation uncertainties on the modelling of the Higgs boson production are evaluated by reweighting the Higgs boson p_{T} distribution. The experimental systematic uncertainty from photon reconstruction is determined with the tag-and-probe method using radiative Z

Table 9: Summary of the statistical and of the main systematic uncertainties on the background estimates, expressed in per cent of the total background yields in each signal region. Uncertainties that are not considered for a particular channel are indicated by a "–". Note that the individual uncertainties can be correlated, and do not necessarily add up quadratically to the total background uncertainty.

	SRℓbb-1	SRℓbb-2	SR$\ell\gamma\gamma$-1	SR$\ell\gamma\gamma$-2	SR$\ell\ell$-1	SR$\ell\ell$-2
Number of background events	6.0 ± 1.3	2.8 ± 0.8	1.6 ± 0.4	3.3 ± 0.8	16.8 ± 2.8	7.3 ± 1.5
Statistical	9	7	22	23	7	7
Modelling $t\bar{t}$	23	25	–	–	< 1	< 1
Modelling single top	5	11	–	–	< 1	< 1
Modelling Wh, Zh, $t\bar{t}h$	–	–	3	1	–	–
Modelling WZ	–	–	–	–	11	22
Electron reconstruction	3	3	1	1	< 1	< 1
Muon reconstruction	1	1	< 1	< 1	1	< 1
Photon reconstruction	–	–	4	5	–	–
Jet energy scale and resolution	6	14	1	3	2	11
b-jet identification	6	4	–	–	–	–
m_{bb} shape	8	12	–	–	–	–
Background $m_{\gamma\gamma}$ model	–	–	5	7	–	–
Non-prompt estimate	–	–	–	–	10	11
Charge mis-measurement estimate	–	–	–	–	2	3
Other sources	4	5	< 1	2	2	2

decays [83].

For the same-sign dilepton channel, the two main sources of systematic uncertainties are related to the non-prompt lepton estimate, and to the modelling of the WZ background. The uncertainty on the non-prompt estimate originates mainly from the limited accuracy of the simulation-to-data scale factors, and on the production rate of non-prompt leptons, in particular their η dependence. The uncertainty on the WZ background modelling is determined using a same-sign, WZ-enriched sample used to validate the Sherpa prediction. This validation sample is selected by requiring three leptons, two of which must have same flavour, opposite sign, $|m_{\ell\ell} - m_Z| < 10$ GeV, and then considering only the highest-p_{T} same-sign pair. None of the other requirements from Table 7 are applied, except for the lepton p_{T} and n_{jet} selections.

9 Results and interpretations

The event yields observed in data are consistent with the Standard Model expectations within uncertainties in all signal regions. The results are used to set exclusion limits with the frequentist hypothesis tests based on the profile log likelihood ratio test statistic and approximated with the asymptotic formulae [84].

Exclusion upper limits at 95% CL on the number of beyond-the-SM (BSM) signal events, S, for each SR are derived using the CL_S prescription [85], assuming no signal yield in other signal and control regions. Normalizing these by the integrated luminosity of the data sample, they can be interpreted as upper limits on the visible BSM cross section, $\sigma_{\mathrm{vis}} = \sigma \times A \times \epsilon$, where σ is the production cross section for the BSM signal, A is the acceptance defined by the fraction of events passing the geometric and kinematic selections at particle level, and ϵ is the detector reconstruction, identification and trigger efficiency.

Table 10 summarizes, for each SR, the observed 95% CL upper limits ($\langle\sigma_{\mathrm{vis}}\rangle^{95}_{\mathrm{obs}}$) of the visible cross section, the observed (S^{95}_{obs}) and expected (S^{95}_{exp}) 95% CL upper limits on the number of signal events with $\pm1\sigma$ excursions of the expectation, the observed confidence level (CL_B) of the background-only hypothesis, and the discovery p-value (p_0), truncated at 0.5.

The obtained results are also used to set exclusion limits on the common mass of the $\tilde{\chi}^{\pm}_1$ and $\tilde{\chi}^0_2$ for various assumptions of the $\tilde{\chi}^0_1$ mass in the simplified model of $pp \to \tilde{\chi}^{\pm}_1\tilde{\chi}^0_2$ followed by $\tilde{\chi}^{\pm}_1 \to W^{\pm}\tilde{\chi}^0_1$

Table 10: From left to right, observed 95% $\mathrm{CL_S}$ upper limits ($\langle\sigma_{\mathrm{vis}}\rangle^{95}_{\mathrm{obs}}$) of the visible cross sections, the observed (S^{95}_{obs}) and expected (S^{95}_{exp}) 95% $\mathrm{CL_S}$ upper limits on the number of signal events with $\pm1\sigma$ excursions of the expectation, the observed confidence level (CL_B) of the background-only hypothesis, and the discovery p-value (p_0), truncated at 0.5.

	$\langle\sigma_{\mathrm{vis}}\rangle^{95}_{\mathrm{obs}}$[fb]	S^{95}_{obs}	S^{95}_{exp}	CL_B	p_0
SRℓbb-1	0.26	5.3	$6.3^{+3.4}_{-2.0}$	0.28	0.50
SRℓbb-2	0.27	5.5	$5.1^{+2.6}_{-1.4}$	0.56	0.43
SR$\ell\gamma\gamma$-1	0.18	3.6	$4.1^{+2.0}_{-0.7}$	0.25	0.50
SR$\ell\gamma\gamma$-2	0.34	7.0	$5.9^{+2.0}_{-1.2}$	0.75	0.19
SR$\ell\ell$-1	0.51	10.4	$10.9^{+3.8}_{-3.1}$	0.51	0.50
SR$\ell\ell$-2	0.51	10.3	$8.1^{+3.3}_{-1.5}$	0.72	0.32

and $\tilde{\chi}_2^0 \rightarrow h\tilde{\chi}_1^0$. In this hypothesis test, all the CRs and SRs of the considered channels are fitted simultaneously, taking into account correlated experimental and theoretical systematic uncertainties as common nuisance parameters. The signal contamination in the CRs is accounted for in the fit, where a single non-negative normalization parameter is used to describe the signal model in all channels.

Systematic uncertainties on the signal expectations stemming from detector effects are included in the fit in the same way as for the backgrounds. Theoretical systematic uncertainties on the signal cross section described in Sec. 3 are not included directly in the fit. In all resulting exclusions the dashed (black) and solid (red) lines show the 95% CL expected and observed limits, respectively, including all uncertainties except for the theoretical signal cross section uncertainty. The (yellow) bands around the expected limits show the $\pm 1\sigma$ expectations. The dotted $\pm 1\sigma$ (red) lines around the

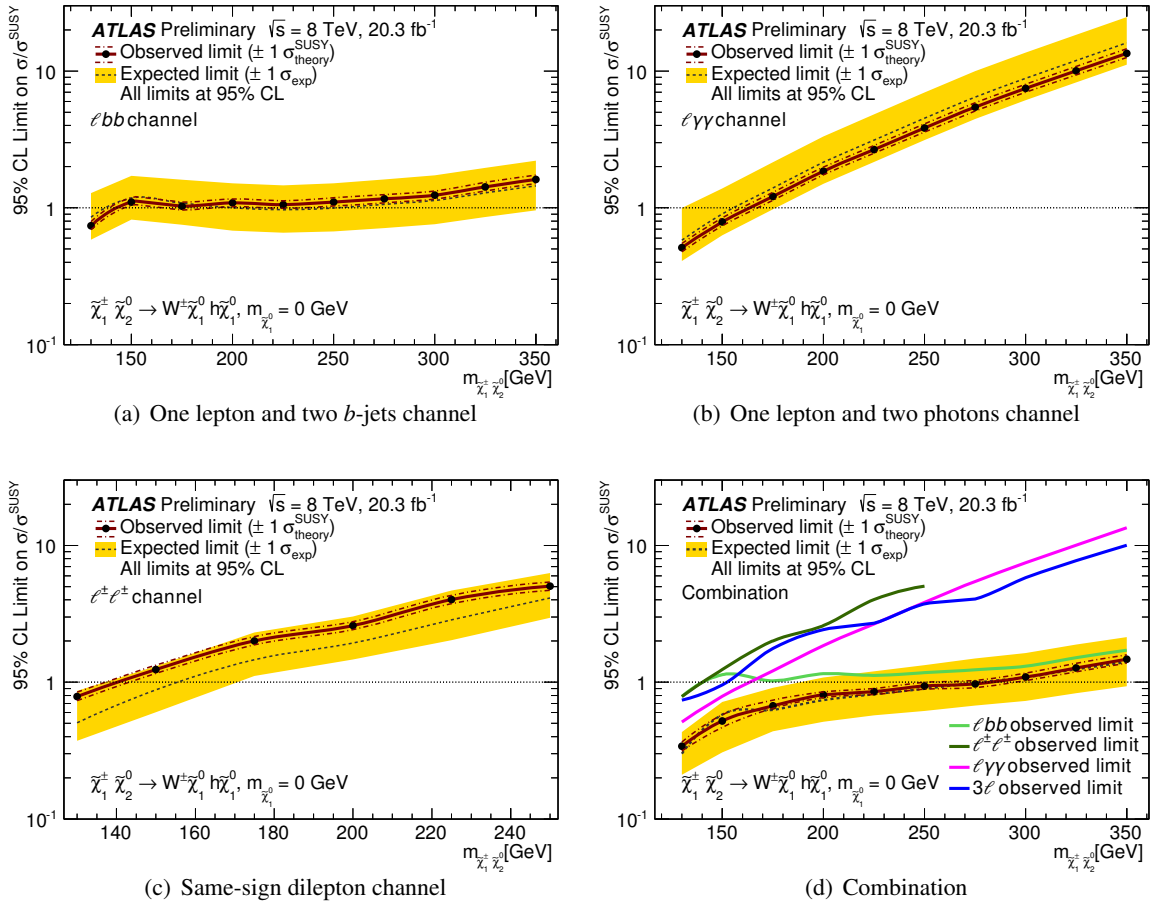

(a) One lepton and two b-jets channel

(b) One lepton and two photons channel

(c) Same-sign dilepton channel

(d) Combination

Figure 7: Observed (solid line) and expected (dashed line) 95% CL upper limits of the cross section normalized by the simplified model prediction for $m_{\tilde{\chi}_1^0} = 0$. The combination in (d) is obtained using the result from the ATLAS three-lepton search [17] in addition to the three channels reported in this note. The $\pm 1\sigma$ lines around the observed limit represent the results obtained when changing the nominal signal cross section up or down by the $\pm 1\sigma$ theoretical uncertainty. The solid band around the expected limit represents the $\pm 1\sigma$ uncertainty band where all uncertainties, except those on the signal cross sections, are considered.

observed limit represent the results obtained when changing the nominal signal cross section up or down by its theoretical uncertainties, and the limits are reported referring to the -1σ variation.

Figure 7 shows the 95% CL upper limits of the signal cross section normalized by the simplified model prediction as a function of $m_{\tilde{\chi}_2^0,\tilde{\chi}_1^\pm}$ for $m_{\tilde{\chi}_1^0} = 0$. The sensitivity of the individual one lepton and two b-jets, one lepton and two photons, and same-sign dilepton channels is illustrated on Figs. 7(a–

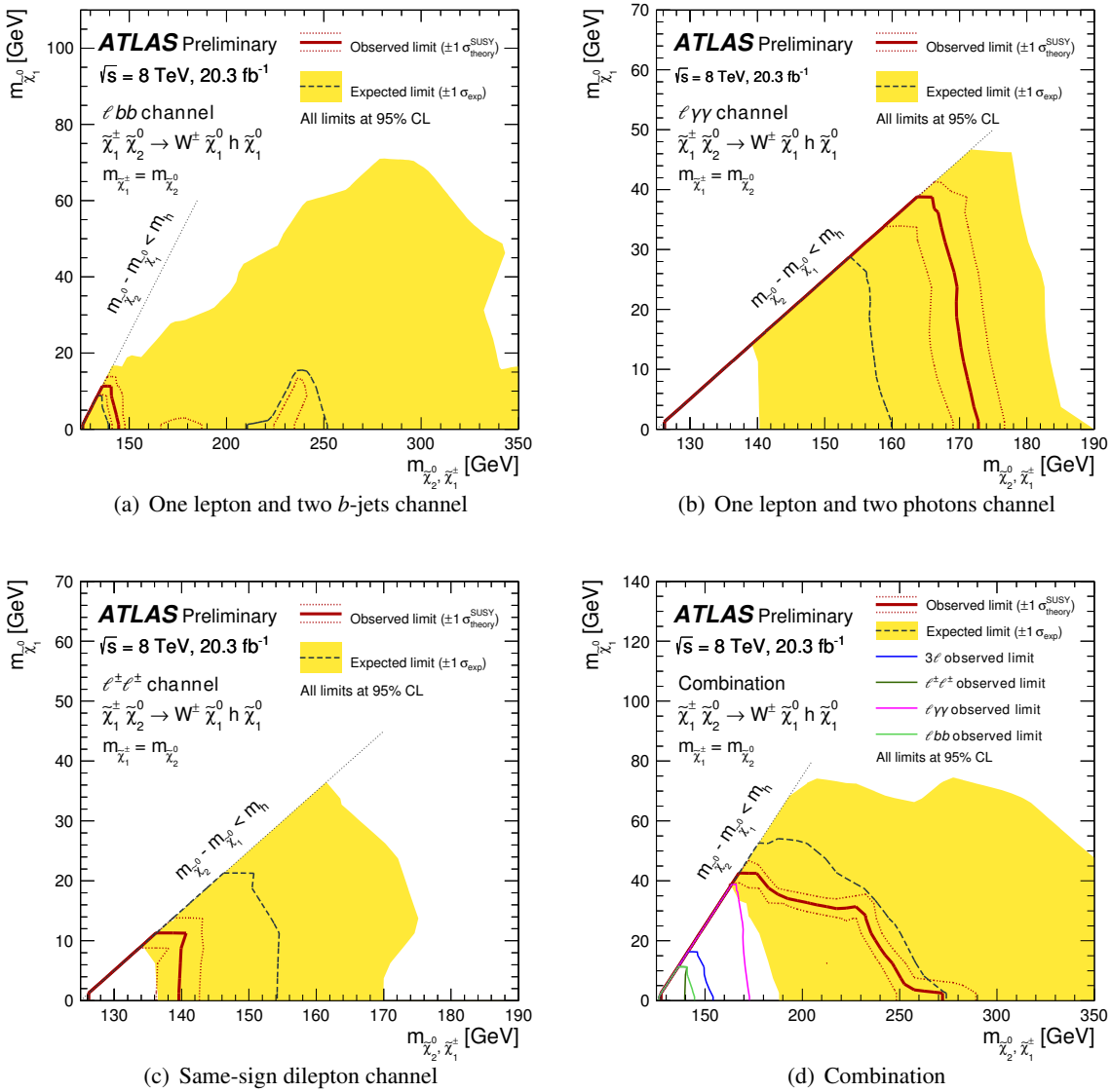

(a) One lepton and two b-jets channel

(b) One lepton and two photons channel

(c) Same-sign dilepton channel

(d) Combination

Figure 8: Observed (solid line) and expected (dashed line) 95% CL exclusion regions in the simplified model. The combination in (d) is obtained using the result from the ATLAS three-lepton search [17] in addition to the three channels reported in this note. The $\pm1\sigma$ lines around the observed limit represent the results obtained when changing the nominal signal cross section up or down by the $\pm1\sigma$ theoretical uncertainty. The solid band around the expected limit shows the $\pm1\sigma$ uncertainty band where all uncertainties, except those on the signal cross sections, are considered.

c), respectively. The corresponding limit combining all channels and the ATLAS three-lepton search is shown in Fig. 7(d). For $m_{\tilde{\chi}_2^0,\tilde{\chi}_1^\pm} > 250$ GeV the same-sign dilepton channel is not considered. In Fig. 7(a), the expected exclusion region below $m_{\tilde{\chi}_2^0,\tilde{\chi}_1^\pm} = 140$ GeV is largely due to SRℓbb-1 that targets models with small mass splitting between the neutralinos, while the expected exclusion region around $m_{\tilde{\chi}_2^0,\tilde{\chi}_1^\pm} = 240$ GeV is driven by SRℓbb-2 designed for larger mass splittings. The upper limit shows slow variation with increasing $m_{\tilde{\chi}_2^0,\tilde{\chi}_1^\pm}$ as the acceptance of SRℓbb-2 increases and compensates the decrease of the production cross section. Figure 7(d) shows that in the $m_{\tilde{\chi}_2^0,\tilde{\chi}_1^\pm} < 170$ GeV range all channels show similar sensitivity, while for $m_{\tilde{\chi}_2^0,\tilde{\chi}_1^\pm} > 170$ GeV the one lepton and two b-jets channel is the dominant one. Nevertheless, the contribution from the other channels to the combination is important to extend the excluded range significantly compared to Fig. 7(a).

Figures 8(a–c) show the 95% CL exclusion regions in the $(m_{\tilde{\chi}_2^0,\tilde{\chi}_1^\pm}, m_{\tilde{\chi}_1^0})$ mass plane of the simplified model obtained from the individual one lepton and two b-jets, one lepton and two photons, and same-sign dilepton signal regions, respectively. Figure 8(d) shows the corresponding exclusion region obtained by combining the three channels described in this note with the ATLAS three-lepton search, which by itself excludes $m_{\tilde{\chi}_2^0,\tilde{\chi}_1^\pm}$ up to 160 GeV for $m_{\tilde{\chi}_1^0} = 0$ GeV as seen in Fig. 8(d). The combination of these four independent searches improves the sensitivity significantly, and the 95% CL exclusion region for $m_{\tilde{\chi}_1^0} = 0$ is extended to 250 GeV. The wide uncertainty bands of the expected limits in Fig. 8 are due to the slow variation of the sensitivity with increasing $m_{\tilde{\chi}_2^0,\tilde{\chi}_1^\pm}$ and $m_{\tilde{\chi}_1^0}$, as can also be seen in Fig. 7.

10 Conclusions

A search for the direct pair production of charginos and neutralinos $pp \to \tilde{\chi}_1^\pm\tilde{\chi}_2^0$ followed by $\tilde{\chi}^\pm \to \tilde{\chi}_1^0(W^\pm \to \ell^\pm\nu)$ and $\tilde{\chi}_2^0 \to \tilde{\chi}_1^0(h \to bb/\gamma\gamma/\ell^\pm\nu qq)$ has been performed using 20.3 fb^{-1} of $\sqrt{s} = 8$ TeV proton–proton collision data delivered by the Large Hadron Collider and recorded with the ATLAS detector. Three final state signatures are considered: one lepton and two b-jets, one lepton and two photons, and two same-sign leptons, each associated with missing transverse momentum. Observations are consistent with the Standard Model expectations. Limits are set in a simplified model, combining these results with the three-lepton search presented in Ref. [17]. For the simplified model, common masses of $\tilde{\chi}_1^\pm$ and $\tilde{\chi}_2^0$ are excluded up to 250 GeV for a massless $\tilde{\chi}_1^0$.

References

[1] H. Miyazawa, *Baryon Number Changing Currents*, Prog. Theor. Phys. **36 (6)** (1966) 1266–1276.

[2] P. Ramond, *Dual Theory for Free Fermions*, Phys. Rev. **D 3** (1971) 2415–2418.

[3] Y. A. Gol'fand and E. P. Likhtman, *Extension of the Algebra of Poincare Group Generators and Violation of p Invariance*, JETP Lett. **13** (1971) 323–326.

[4] A. Neveu and J. H. Schwarz, *Factorizable dual model of pions*, Nucl. Phys. **B 31** (1971) 86–112.

[5] A. Neveu and J. H. Schwarz, *Quark Model of Dual Pions*, Phys. Rev. **D 4** (1971) 1109–1111.

[6] J. Gervais and B. Sakita, *Field theory interpretation of supergauges in dual models*, Nucl. Phys. **B 34** (1971) 632–639.

[7] D. V. Volkov and V. P. Akulov, *Is the Neutrino a Goldstone Particle?*, Phys. Lett. **B 46** (1973) 109–110.

[8] J. Wess and B. Zumino, *A Lagrangian Model Invariant Under Supergauge Transformations*, Phys. Lett. **B 49** (1974) 52–54.

[9] J. Wess and B. Zumino, *Supergauge Transformations in Four-Dimensions*, Nucl. Phys. **B 70** (1974) 39–50.

[10] P. Fayet, *Supersymmetry and Weak, Electromagnetic and Strong Interactions*, Phys. Lett. **B 64** (1976) 159–162.

[11] P. Fayet, *Spontaneously Broken Supersymmetric Theories of Weak, Electromagnetic and Strong Interactions*, Phys. Lett. **B 69** (1977) 489–494.

[12] G. R. Farrar and P. Fayet, *Phenomenology of the Production, Decay, and Detection of New Hadronic States Associated with Supersymmetry*, Phys. Lett. **B 76** (1978) 575–579.

[13] P. Fayet, *Relations Between the Masses of the Superpartners of Leptons and Quarks, the Goldstino Couplings and the Neutral Currents*, Phys. Lett. **B 84** (1979) 416–420.

[14] R. Barbieri and G. Giudice, *Upper Bounds on Supersymmetric Particle Masses*, Nucl. Phys. **B 306** (1988) 63–76.

[15] B. de Carlos and J. A. Casas, *One loop analysis of the electroweak breaking in supersymmetric models and the fine tuning problem*, Phys. Lett. **B 309** (1993) 320–328, hep-ph/9303291.

[16] J. Alwall et al., *Simplified Models for a First Characterization of New Physics at the LHC*, Phys. Rev. **D 79** (2009) 075020, arXiv:0810.3921 [hep-ph].

[17] ATLAS Collaboration, *Search for direct production of charginos and neutralinos in events with three leptons and missing transverse momentum in* $\sqrt{s} = 8$*TeV pp collisions with the ATLAS detector*, JHEP **1404** (2014) 169, arXiv:1402.7029 [hep-ex].

[18] ATLAS Collaboration, *Search for direct production of charginos, neutralinos and sleptons in final states with two leptons and missing transverse momentum in pp collisions at* $\sqrt{s} = 8$ *TeV with the ATLAS detector*, JHEP **1405** (2014) 071, arXiv:1403.5294 [hep-ex].

[19] ATLAS Collaboration, *Search for the direct production of charginos, neutralinos and staus in final states with at least two hadronically decaying taus and missing transverse momentum in pp collisions at* $\sqrt{s} = 8$ *TeV with the ATLAS detector*, arXiv:1407.0350 [hep-ex].

[20] CMS Collaboration, *Searches for electroweak production of charginos, neutralinos, and sleptons decaying to leptons and W, Z, and Higgs bosons in pp collisions at 8 TeV*, Eur. Phys. J. **C74** no. 9, (2014) 3036, arXiv:1405.7570 [hep-ex].

[21] CMS Collaboration, *Searches for electroweak neutralino and chargino production in channels with Higgs, Z, and W bosons in pp collisions at 8 TeV*, arXiv:1409.3168 [hep-ex].

[22] D0 Collaboration, V. Abazov, et al., *Search for associated production of charginos and neutralinos in the trilepton final state using 2.3* fb^{-1} *of data*, Phys. Lett. **B 680** (2009) 34–43, arXiv:0901.0646 [hep-ex].

[23] CDF Collaboration, T. Aaltonen, et al., *Search for Supersymmetry in $p\bar{p}$ Collisions at $\sqrt{s}$ = 1.96-TeV Using the Trilepton Signature of Chargino-Neutralino Production*, Phys. Rev. Lett. **101** (2008) 251801, arXiv:0808.2446 [hep-ex].

[24] LEPSUSYWG, ALEPH, DELPHI, L3 and OPAL experiments, *Combined LEP Chargino Results up to* 208 GeV *for large m0*, LEPSUSYWG/01-03.1. http://lepsusy.web.cern.ch/lepsusy/Welcome.html.

[25] ALEPH Collaboration, S. Schael, et al., *Absolute mass lower limit for the lightest neutralino of the MSSM from e^+e^- data at $\sqrt{s}$ up to 209 GeV*, Phys. Lett. **B 583** (2004) 247–263.

[26] DELPHI Collaboration, J. Abdallah, et al., *Searches for supersymmetric particles in e^+e^- collisions up to 208-GeV and interpretation of the results within the MSSM*, Eur.Phys.J. **C31** (2003) 421–479, arXiv:hep-ex/0311019 [hep-ex].

[27] L3 Collaboration, M. Acciarri, et al., *Search for charginos and neutralinos in e^+e^- collisions at $\sqrt{s}$ = 189 GeV*, Phys. Lett. **B 472** (2000) 420–433, hep-ex/9910007.

[28] OPAL Collaboration, G. Abbiendi, et al., *Search for chargino and neutralino production at $\sqrt{s}$ = 192 GeV to 209 GeV at LEP*, Eur. Phys. J. **C 35** (2004) 1–20, hep-ex/0401026.

[29] ATLAS Collaboration, *The ATLAS Experiment at the CERN Large Hadron Collider*, JINST **3** (2008) S08003.

[30] GEANT4 Collaboration, S. Agostinelli, et al., *GEANT4: A simulation toolkit*, Nucl. Instrum. Meth. **A 506** (2003) 250–303.

[31] ATLAS Collaboration, *The ATLAS Simulation Infrastructure*, Eur. Phys. J. **C 70** (2010) 823–874, arXiv:1005.4568 [physics.ins-det].

[32] ATLAS Collaboration, *The simulation principle and performance of the ATLAS fast calorimeter simulation FastCaloSim*, ATL-PHYS-PUB-2010-013 (2010). http://cdsweb.cern.ch/record/1300517.

[33] T. Sjostrand, S. Mrenna, and P. Z. Skands, *A Brief Introduction to PYTHIA 8.1*, Comput.Phys.Commun. **178** (2008) 852–867, arXiv:0710.3820 [hep-ph]. Version 8.160.

[34] B. P. Kersevan and E. Richter-Was, *The Monte Carlo event generator AcerMC versions 2.0 to 3.8 with interfaces to PYTHIA 6.4, HERWIG 6.5 and ARIADNE 4.1*, Comput. Phys. Commun. **184** no. 3, (2013) 919 – 985. Version 38.

[35] T. Sjostrand, S. Mrenna, and P. Z. Skands, *PYTHIA 6.4 Physics and Manual*, JHEP **05** (2006) 026, arXiv:hep-ph/0603175. Version 6.426.

[36] N. Kidonakis, *Next-to-next-to-leading-order collinear and soft gluon corrections for t-channel single top quark production*, Phys. Rev. **D 83** (2011) 091503, arXiv:1103.2792 [hep-ph].

[37] ATLAS Collaboration, *ATLAS tunes of PYTHIA 6 and Pythia 8 for MC11*, ATL-PHYS-PUB-2011-009 (2011). http://cdsweb.cern.ch/record/1363300.

[38] J. Pumplin et al., *New generation of parton distributions with uncertainties from global QCD analysis*, JHEP **07** (2002) 012, hep-ph/0201195.

[39] P. Nason, *A New method for combining NLO QCD with shower Monte Carlo algorithms*, JHEP **11** (2004) 040, hep-ph/0409146. Version r1556.

[40] S. Frixione, P. Nason, and C. Oleari, *Matching NLO QCD computations with Parton Shower simulations: the POWHEG method*, JHEP **11** (2007) 070, arXiv:0709.2092 [hep-ph].

[41] N. Kidonakis, *NNLL resummation for s-channel single top quark production*, Phys. Rev. **D 81** (2010) 054028, arXiv:1001.5034 [hep-ph].

[42] P. Z. Skands, *Tuning Monte Carlo Generators: The Perugia Tunes*, Phys. Rev. **D82** (2010) 074018, arXiv:1005.3457 [hep-ph].

[43] H.-L. Lai et al., *New parton distributions for collider physics*, Phys. Rev. **D 82** (2010) 074024, arXiv:1007.2241 [hep-ph].

[44] N. Kidonakis, *Two-loop soft anomalous dimensions for single top quark associated production with a W- or H-*, Phys. Rev. **D 82** (2010) 054018, arXiv:1005.4451 [hep-ph].

[45] M. Cacciari et al., *Top-pair production at hadron colliders with next-to-next-to-leading logarithmic soft-gluon resummation*, Phys. Lett. **B 710** (2012) 612–622, arXiv:1111.5869 [hep-ph].

[46] P. Baernreuther, M. Czakon, and A. Mitov, *Percent Level Precision Physics at the Tevatron: First Genuine NNLO QCD Corrections to $q\bar{q} \to t\bar{t} + X$*, Phys. Rev. Lett. **109** (2012) 132001, arXiv:1204.5201 [hep-ph].

[47] M. Czakon and A. Mitov, *NNLO corrections to top-pair production at hadron colliders: the all-fermionic scattering channels*, JHEP **12** (2012) 054, arXiv:1207.0236 [hep-ph].

[48] M. Czakon and A. Mitov, *NNLO corrections to top pair production at hadron colliders: the quark-gluon reaction*, JHEP **01** (2013) 080, arXiv:1210.6832 [hep-ph].

[49] M. Czakon, P. Fiedler, and A. Mitov, *The total top quark pair production cross-section at hadron colliders through $O(\alpha_S^4)$*, Phys. Rev. Lett. **110** (2013) 252004, arXiv:1303.6254 [hep-ph].

[50] M. Czakon and A. Mitov, *Top++: A Program for the Calculation of the Top-Pair Cross-Section at Hadron Colliders*, arXiv:1112.5675 [hep-ph].

[51] J. Alwall et al., *MadGraph/MadEvent v4: The New Web Generation*, JHEP **09** (2007) 028, arXiv:0706.2334 [hep-ph]. Version 1.5.2.

[52] T. Gleisberg et al., *Event generation with SHERPA 1.1*, JHEP **02** (2009) 007, arXiv:0811.4622 [hep-ph]. Version 1.4.1.

[53] M. L. Mangano et al., *ALPGEN, a generator for hard multiparton processes in hadronic collisions*, JHEP **07** (2003) 001, hep-ph/0206293. Version 2.14.

[54] S. Heinemeyer et al., *Handbook of LHC Higgs Cross Sections: 3. Higgs Properties*, arXiv:1307.1347 [hep-ph].

[55] ATLAS Collaboration, *Summary of ATLAS Pythia 8 tunes*, ATL-PHYS-PUB-2012-003 (2012). http://cdsweb.cern.ch/record/1474107.

[56] M. Bahr et al., *Herwig++ Physics and Manual*, Eur. Phys. J. **C 58** (2008) 639–707, arXiv:0803.0883 [hep-ph].

[57] W. Beenakker et al., *Squark and gluino production at hadron colliders*, Nucl. Phys. **B 492** (1997) 51–103, hep-ph/9610490.

[58] B. Fuks, M. Klasen, D. R. Lamprea, and M. Rothering, *Gaugino production in proton-proton collisions at a center-of-mass energy of 8 TeV*, JHEP **10** (2012) 081, arXiv:1207.2159 [hep-ph].

[59] B. Fuks, M. Klasen, D. R. Lamprea, and M. Rothering, *Precision predictions for electroweak superpartner production at hadron colliders with Resummino*, Eur. Phys. J. **C 73** (2013) 2480, arXiv:1304.0790 [hep-ph].

[60] M. Kramer et al., *Supersymmetry production cross sections in pp collisions at* $\sqrt{s} = 7$ *TeV*, arXiv:1206.2892 [hep-ph].

[61] ATLAS Collaboration, *Improved luminosity determination in pp collisions at* $\sqrt{s} = 7$ *TeV using the ATLAS detector at the LHC*, Eur. Phys. J. **C73** (2013) 2518, arXiv:1302.4393 [hep-ex].

[62] ATLAS Collaboration, *Electron reconstruction and identification efficiency measurements with the ATLAS detector using the 2011 LHC proton-proton collision data*, Eur. Phys. J. **C74** (2014) 2941, arXiv:1404.2240 [hep-ex].

[63] ATLAS Collaboration, *Measurement of the muon reconstruction performance of the ATLAS detector using 2011 and 2012 LHC proton-proton collision data*, CERN-PH-EP-2014-151 (2014), arXiv:1407.3935 [hep-ex].

[64] A. Collaboration, *Electron and photon energy calibration with the ATLAS detector using LHC Run 1 data*, Eur. Phys. J. **C74** no. 10, (2014) 3071, arXiv:1407.5063 [hep-ex].

[65] M. Cacciari, G. P. Salam, and G. Soyez, *The anti-k_t jet clustering algorithm*, JHEP **04** (2008) 063, arXiv:0802.1189 [hep-ph].

[66] W. Lampl et al., *Calorimeter clustering algorithms: Description and performance*, ATL-LARG-PUB-2008-002 (2008). http://cdsweb.cern.ch/record/1099735.

[67] ATLAS Collaboration, *Jet energy measurement with the ATLAS detector in proton-proton collisions at* $\sqrt{s} = 7$ *TeV*, Eur. Phys. J. **C 73** (2013) 2304, arXiv:1112.6426 [hep-ex].

[68] ATLAS Collaboration, *Jet energy measurement and its systematic uncertainty in proton-proton collisions at* $\sqrt{s} = 7$ *TeV with the ATLAS detector*, arXiv:1406.0076 [hep-ex].

[69] ATLAS collaboration, *Pile-up subtraction and suppression for jets in ATLAS*, ATLAS-CONF-2013-083 (2013). http://cdsweb.cern.ch/record/1570994.

[70] ATLAS Collaboration, *Commissioning of the ATLAS high-performance b-tagging algorithms in the 7 TeV collision data*, ATLAS-CONF-2011-102 (2011). http://cdsweb.cern.ch/record/1369219.

[71] ATLAS Collaboration, *Determination of the tau energy scale and the associated systematic uncertainty in proton-proton collisions at* $\sqrt{s} = 8$ *TeV with the ATLAS detector at the LHC in 2012*, ATL-PHYS-PUB-2013-044 (2013). http://cdsweb.cern.ch/record/1544036.

[72] ATLAS Collaboration, *Performance of missing transverse momentum reconstruction in proton-proton collisions at 7 TeV with ATLAS*, Eur. Phys. J. **C 72** (2012) 1844, arXiv:1108.5602 [hep-ex].

[73] ATLAS Collaboration, *Performance of Missing Transverse Momentum Reconstruction in ATLAS studied in Proton-Proton Collisions recorded in 2012 at 8 TeV*, ATLAS-CONF-2013-082 (2013). http://cdsweb.cern.ch/record/1570993.

[74] D. R. Tovey, *On measuring the masses of pair-produced semi-invisibly decaying particles at hadron colliders*, JHEP **0804** (2008) 034, arXiv:0802.2879 [hep-ph].

[75] G. Polesello and D. R. Tovey, *Supersymmetric particle mass measurement with the boost-corrected contransverse mass*, JHEP **1003** (2010) 030, arXiv:0910.0174 [hep-ph].

[76] M. Baak et al., *HistFitter software framework for statistical data analysis*, arXiv:1410.1280 [hep-ex].

[77] ATLAS Collaboration, *Measurements of Higgs boson production and couplings in diboson final states with the ATLAS detector at the LHC*, Phys. Lett. **B726** (2013) 88–119, arXiv:1307.1427 [hep-ex].

[78] ATLAS Collaboration, *Search for new phenomena in events with three charged leptons at* $\sqrt{s} = 7$ TeV *with the ATLAS detector*, Phys. Rev. D **87** (2013) 052002. http://link.aps.org/doi/10.1103/PhysRevD.87.052002.

[79] M. Oreglia, *A Study of the Reactions* $\psi' \to \gamma\gamma\psi$, SLAC-R-0236 (1980).

[80] ATLAS Collaboration, *Search for supersymmetry at* $\sqrt{s}$*=8 TeV in final states with jets and two same-sign leptons or three leptons with the ATLAS detector*, JHEP **1406** (2014) 035, arXiv:1404.2500 [hep-ex].

[81] ATLAS Collaboration, *Jet energy resolution in proton-proton collisions at* $\sqrt{s} = 7$ *TeV recorded in 2010 with the ATLAS detector*, Eur.Phys.J. **C73** (2013) 2306, arXiv:1210.6210 [hep-ex].

[82] ATLAS collaboration, *Calibration of b-tagging using dileptonic top pair events in a combinatorial likelihood approach with the ATLAS experiment*, ATLAS-CONF-2014-004 (2014). http://cdsweb.cern.ch/record/1664335.

[83] ATLAS Collaboration, *Measurements of the photon identification efficiency with the ATLAS detector using 4.9* fb^{-1} *of pp collision data collected in 2011*, ATLAS-CONF-2012-123 (2012). http://cdsweb.cern.ch/record/1473426.

[84] G. Cowan et al., *Asymptotic formulae for likelihood-based tests of new physics*, Eur. Phys. J. **C 71** (2011) 1554, arXiv:1007.1727 [physics.data-an].

[85] A. L. Read, *Presentation of search results: The CL(s) technique*, J. Phys. **G 28** (2002) 2693–2704.